applied sciences

MDPI

Article

Chamber-Reflection-Aware Image Enhancement Method for Powder Spreading Quality Inspection in Selective Laser Melting

Zhenxing Huang [1,2,*], Changfeng Yan [1] and Siwei Yang [3]

[1] School of Mechanical and Electrical Engineering, Lanzhou University of Technology, Lanzhou 730050, China; changf_yan@163.com
[2] Luoyang Aurora Precision Manufacturing Co., Ltd., Luoyang 471000, China
[3] School of Information Technology, Tsinghua University, Beijing 100080, China
* Correspondence: huangzxmee@163.com

Abstract

In selective laser melting (SLM), real-time visual inspection of powder spreading quality is essential for maintaining dimensional accuracy and mechanical performance. However, reflections from metallic chamber walls introduce non-uniform illumination and reduce local contrast, hindering reliable defect detection. To overcome this problem, a chamber-reflection-aware image enhancement method is proposed, integrating a physical reflection model with a dual-channel deep network. A Gaussian-based curved-surface reflection model is first developed to describe the spatial distribution of reflective interference. The enhancement network then processes the input through two complementary channels: a Retinex-based branch to extract illumination-invariant reflectance components and a principal components analysis (PCA)-based branch to preserve structural information. Furthermore, a noise-aware loss function is designed to suppress the mixed Gaussian–Poisson noise that is inherent in SLM imaging. Experiments conducted on real SLM monitoring data demonstrate that the proposed method significantly improves contrast and defect visibility, outperforming existing enhancement algorithms in peak signal-to-noise ratio (PSNR), structural similarity index (SSIM), and natural image quality evaluator (NIQE). The approach provides a physically interpretable and robust preprocessing framework for online SLM quality monitoring.

Keywords: selective laser melting; chamber reflection; image enhancement; Retinex; deep learning

Check for updates

Academic Editors: Antonio Fernández-Caballero and Byung-Gyu Kim

Received: 22 November 2025
Revised: 12 December 2025
Accepted: 18 December 2025
Published: 24 December 2025

Copyright: © 2025 by the authors. Licensee MDPI, Basel, Switzerland. This article is an open access article distributed under the terms and conditions of the Creative Commons Attribution (CC BY) license.

1. Introduction

Selective Laser Melting (SLM) has been widely applied in aerospace, medical, and related industries owing to its ability to fabricate geometrically complex components directly [1]. The quality of powder spreading significantly affects the performance of the final parts; therefore, accurate real-time detection of spreading defects is essential [2]. However, SLM still encounters challenges, such as limited process stability, inadequate real-time quality monitoring, and underdeveloped online parameter control methods [3]. Continuous defect monitoring and prompt feedback to the manufacturing system are considered crucial for improving overall quality control.

Visual inspection has attracted considerable attention as a non-contact, high-resolution method for assessing powder spreading quality [4]. However, commercial SLM systems often exhibit non-uniform illumination in powder bed images due to reflections from metallic

chamber walls. This issue arises from design tradeoffs made to ensure structural integrity and atmospheric purity under high-temperature conditions. Uncoated metallic chamber walls are generally used because they endure thermal cycling and mechanical stress while preventing contamination that could result from coatings [5,6]. Recent studies in other imaging domains, such as underwater and structural monitoring, have demonstrated the effectiveness of Retinex-based decomposition and principal component analysis (PCA) in handling complex illumination and structural degradation [7–15]. These methods provide valuable insights for SLM image enhancement, particularly in separating reflective artifacts from meaningful structural information [16]. In addition, their high thermal conductivity supports uniform temperature fields (typically 80–200 °C), which are essential for achieving desired alloy heat-treatment properties. Metallic powder particles also tend to splash onto chamber walls during spreading. Therefore, smooth metallic surfaces are preferred to prevent powder accumulation, a critical safety consideration since rough or coated surfaces could retain excessive powder and create serious industrial hazards. Consequently, smooth metallic chamber walls are regarded as the optimal design, ensuring both effective thermal management and process safety.

Nevertheless, this design introduces substantial challenges. The high reflectivity of metallic materials, particularly when processing reflective alloys, such as copper, remained a major technological limitation [17,18]. Hardware-based solutions, including modifications to chamber wall properties or the use of specialized-wavelength lasers, are expensive and may introduce new process risks. Consequently, image enhancement algorithms were considered a more practical and universal approach, enabling optical compensation for chamber-wall reflections through post-processing [19,20].

Chamber-wall reflections cause brightness nonuniformity and reduced contrast in powder bed images, significantly impairing both visual and automated defect detection. This issue is widespread [21,22]. In the in-process monitoring of Selective Laser Melting (SLM), establishing quantitative correlations between monitoring signals and defects is one of the central objectives of intelligent monitoring, and the accuracy of such correlations is directly constrained by image quality [23].

Similarly, Identified metallic surface and powder reflections as major interference sources in optical monitoring, leading to localized over-exposure and detail loss, confirming the severity and ubiquity of this problem [24,25].

Among available SLM defect monitoring methods (optical, acoustic, and thermal), vision-based optical techniques are most extensively studied due to their high information content and low equipment cost. However, current methods remain insufficient for accurately modeling and correcting complex image degradation induced by manufacturing conditions, such as curved chamber-wall reflections [26]. Furthermore, despite the transition of additive manufacturing from prototyping to the direct production of complex components, real-time monitoring and adaptive control technologies remain immature [3].

To address challenges arising from chamber-wall reflections, current research primarily focuses on three approaches.

Hardware optimization (e.g., multi-angle illumination [23] or polarizing filters [25]) mitigates reflections at the source but entails high costs and is constrained by process conditions.

Traditional image enhancement algorithms (e.g., homomorphic filtering and multi-scale Retinex (MSR) [27,28]) often provide limited suppression and may amplify noise or distort structural details when processing strong structured reflections and metallic powder noise in SLM images.

Deep learning-based enhancement methods (e.g., EnlightenGAN) exhibit strong data-driven learning capabilities but fail to adequately correct localized strong reflections in SLM images and lack integration of physical principles.

Notably, the integration of physical models with deep learning has emerged as a promising paradigm for industrial vision tasks [2]. Wu et al. [19]. developed URetinex-Net, an unfolding-based optimization framework that embeds the Retinex physical model into neural networks, improving interpretability and establishing a key benchmark. Li et al. [27]. further incorporated explicit noise terms to construct robust Retinex models, effectively mitigating noise amplification. These studies confirm the value of embedding domain knowledge as strong priors, offering crucial methodological guidance for this work [29,30].

However, despite the progress achieved by existing Retinex-based and deep learning enhancement approaches, their direct application to SLM powder-spreading images still faces persistent and unresolved challenges:

(1) Insufficient physical modeling remains a fundamental limitation. Existing studies lack a parameterized and process-specific physical model capable of describing the spatially varying reflective behavior of curved metallic chamber walls in SLM systems [17,18,31]. Without an explicit model of chamber-wall illumination attenuation, current methods cannot accurately estimate or correct the non-uniform reflections intrinsic to SLM imaging.

(2) Inadequate continues to hinder performance. Prior studies rarely incorporate a noise model tailored to the mixed Poisson–Gaussian characteristics originating from metallic powders and sCMOS sensors. As a result, existing enhancement algorithms struggle to suppress high-frequency metallic powder noise while preserving defect-relevant structures, particularly under low-illumination conditions [32–34].

(3) A decomposition balance dilemma persists in Retinex-based methods. Conventional Retinex formulations often fail to maintain an optimal trade-off between illumination smoothing and texture/detail preservation in SLM scenarios, leading to over-smoothing or structural distortion [19,27,28]. At the same time, current deep learning approaches do not provide a physically guided integration of Retinex decomposition with PCA-based structural preservation, leaving the decomposition process insufficiently constrained by physical principles.

Together, these limitations highlight three critical research gaps:

(1) The absence of a parameterized chamber-reflection model tailored for SLM;
(2) The lack of a noise model addressing Poisson–Gaussian mixed noise in metallic powder images;
(3) The absence of a physics-guided integration of Retinex and PCA for balanced illumination–structure decomposition.

To overcome these limitations, this study proposes a novel image enhancement algorithm that integrates a physical model of chamber-wall reflections with a dual-channel deep decomposition network. Guided by physics-based modeling, the method employs Retinex and principal components analysis (PCA) dual-channel decomposition to effectively separate illumination components from reflection components containing structural details. A metal-noise-aware loss function is introduced to jointly optimize the suppression of chamber-wall reflections and complex noise while enhancing the visibility of powder spreading defects.

2. Experimental Methodology

2.1. Datasets, Platform, and Evaluation System

The constructed dataset comprises 4200 high-resolution powder spreading images acquired from commercial, in-house, and large-format selective laser melting systems, including the BLT-S600 (Xi'an Bright Laser Technologies Co., Ltd., Xi'an, China), EOS M290 (EOS GmbH, Krallling, Germany), and SLM Solutions 280 HL (SLM Solutions

Group AG, Lübeck, Germany). It systematically captures variations across the following key dimensions:

- Image Zoning: According to the measured illumination profile, the powder bed was categorized into three characteristic zones (Figure 1c): Central Zone (1890 images), Transition Zone (1260 images), and Edge Reflection Zone (1050 images). This distribution accounts for the larger physical area of the central region while ensuring adequate representation of the edge zone, where reflective interference is most severe, to robustly train the model for extreme image degradation.

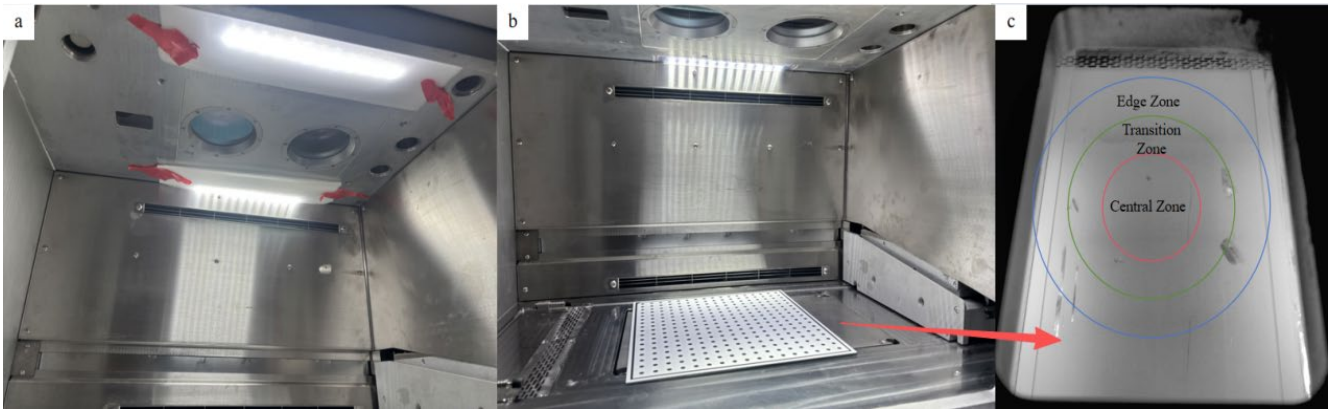

Figure 1. Schematic of the experimental setup and the resulting illumination zones on the powder bed. (**a**) The imaging setup features two linear light sources and an sCMOS camera installed on the upper chamber wall. (**b**) Illustration of the chamber-wall reflection phenomenon influencing powder bed visibility. (**c**) Illumination zonation map, dividing the powder bed into three distinct regions to delineate reflection intensity: the Edge Reflection Zone (subject to strong specular reflections), the Transition Zone (moderately and uniformly illuminated), and the Central Zone (predominantly under ambient diffuse illumination).

- Build Platform Sizes: $260 \times 260 \times 300\ mm^3$, $250 \times 350 \times 325\ mm^3$ and $280 \times 280 \times 365\ mm^3$.
- Powder Materials: 316L stainless steel, TC4 titanium alloy, and AlSi10Mg aluminum alloy, with particle sizes ranging from 15 to 45 μm.
- Process Parameters: Chamber oxygen levels were maintained between 0.3% and 0.5%, with layer thicknesses varying from 30 to 60 μm (detailed parameters are provided in Table 1).

Table 1. SLM Process Parameters.

Material Type	Parameter Type	Laser Power (w)	Scan Speed (mm/s)	Layer Thickness (mm)
TC4	Bottom Surface	120	1100	0.03
	Bottom Surface Contour	100	1250	
	Main Body	280	1100	
	Main Body Contour	150	700	
	Top Surface	260	1300	
	Top Surface Contour	150	700	
	Support Structures	350	1150	
316L	Bottom Surface	150	1000	0.06
	Bottom Surface Contour	120	1600	
	Main Body	350	900	
	Main Body Contour	160	400	
	Top Surface	168	600	
	Top Surface Contour	150	750	
	Support Structures	350	1150	

Table 1. *Cont.*

Material Type	Parameter Type	Laser Power (w)	Scan Speed (mm/s)	Layer Thickness (mm)
AlSi10Mg	Bottom Surface	200	1200	0.04
	Bottom Surface Contour	180	1400	
	Main Body	300	1300	
	Main Body Contour	200	800	
	Top Surface	280	1400	
	Top Surface Contour	200	800	
	Support Structures	320	1200	

- Illumination Schemes: Various configurations were included, such as top-mounted dual linear lights, four-corner distributed LEDs, and integrated ring lighting.
- Defect Types: Representative anomalies, including doctor blade scratches, insufficient powder spreading, and powder agglomeration.

For the primary imaging system, an industrial-grade sCMOS camera paired with two linear light sources was mounted on the upper chamber wall (Figure 1a,b) to ensure acquisition accuracy. Images from other systems were obtained using their native in situ monitoring cameras under standard process lighting.

To bolster the model's adaptability to unseen scenarios, an extensive data augmentation pipeline was implemented during training. This included:

- Geometric Transformations: Random rotation $(\pm 10^{\circ})$, scaling $(0.9 - 1.1)$, and horizontal/vertical flipping.
- Photometric Variations: Brightness $(\pm 20\%)$ and contrast $(\pm 15\%)$ adjustments, along with simulated glare overlay using Gaussian kernels to replicate unseen reflection patterns.
- Synthetic Noise Injection: Mixed Poisson–Gaussian noise with signal-dependent variance was added to emulate sensor noise under low-light conditions.

This multi-source, multi-condition dataset, complemented by systematic augmentation, ensures exposure of the trained model to a broad spectrum of real-world imaging variations. Consequently, it enhances the model's generalization capability across different SLM machines, material reflectivities, and illumination geometries.

For model development, the dataset was randomly partitioned into training, validation, and test sets at a 70:15:15 ratio. Stratified sampling was employed to maintain a balanced representation of machine source, material type, illumination condition, and defect category across all subsets, thereby ensuring the statistical representativeness and generalizability of the evaluation.

To uphold experimental reliability and industrial relevance, the imaging system design and evaluation procedures adhered to established industrial vision standards. Compliance with illumination uniformity (ISO 14524:2009 [35]), camera calibration (EMVA 1288:2023 [36]), and additive manufacturing process documentation (ASTM F3303-20 [37]) norms ensured consistent image acquisition, reproducible measurements, and traceable parameter recording throughout the study.

To ensure full reproducibility, we detail the complete training procedure and hyperparameters. The model was implemented in PyTorch 1.12.1 and trained on a workstation with an NVIDIA RTX 3090 GPU (24 GB memory) and an Intel Core i9-12900K CPU. The dataset was split as follows: 2940 images for training (model weight updates), 630 for validation (monitoring and early stopping), and 630 for final independent testing.

Training was conducted for 300 epochs with a batch size of 8, using the Adam optimizer at an initial learning rate of 1×10^{-4}. The learning rate was halved every 50 epochs following a step-decay schedule. The metal noise-aware total loss (defined in Section 2.4)

was used as the objective function. Both training and validation losses decreased smoothly throughout the process, converging stably without indication of overfitting. The final model for testing was selected from the checkpoint that achieved the lowest validation loss.

2.2. Degradation Mechanism and Quantitative Analysis of SLM Powder Spreading Images

The degradation of SLM powder spreading images primarily results from chamber-wall reflections, appearing as non-uniform illumination coupled with metallic powder noise. According to surface optics theory, a Gaussian attenuation model was adopted to describe the spatial distribution of reflections (Figure 2). The model is mathematically expressed as follows:

$$L_{wall}(x, y) = k \cdot \left(1 - e^{-\frac{(x-x_c)^2+(y-y_c)^2}{2\sigma^2}}\right), \quad (1)$$

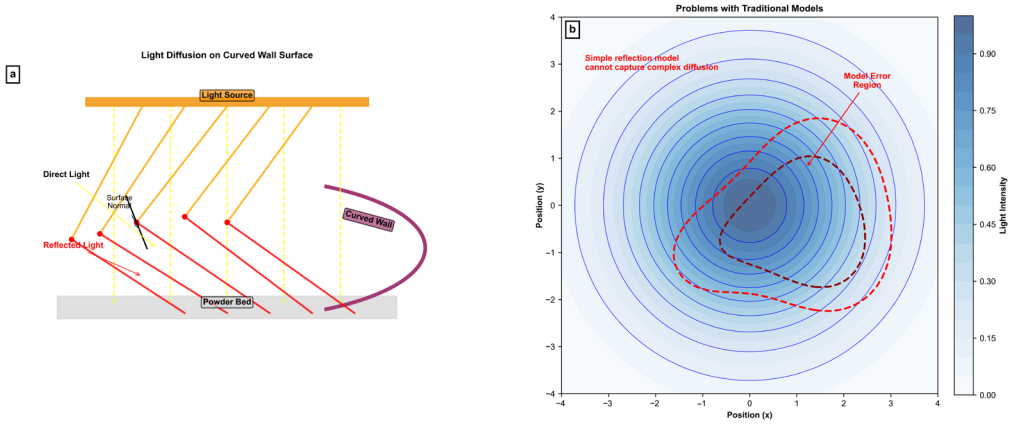

Figure 2. Chamber-wall reflection behavior and its modeling. (**a**) Complex light diffusion on a curved chamber wall. (**b**) Schematic of modeling errors in traditional approaches. The adopted reflection attenuation model, which follows a Gaussian form (Equation (1)). The key parameters are the platform center coordinates (x_c, y_c), the reflection diffusion coefficient σ, and the light intensity coefficient k, all of which were obtained by fitting to experimental measurements.

The parameters (k, σ, x_c, y_c) of the Gaussian attenuation model in Equation (1) were determined through a systematic, three-step calibration procedure. This process fits a continuous physical model to discretely sampled intensity data as described below.

(1) Data Acquisition: A standard white diffuse reflectance target was placed on the build platform. Under the same lighting conditions used for in situ SLM monitoring, a series of images were captured by the sCMOS camera. Pixel coordinates (x_i, y_i) and their corresponding intensities I_i within the platform region were extracted to form a discrete intensity dataset $\{(x_i, y_i, I_i)\}_{i=1}^{N}$. This dataset characterizes the spatial intensity distribution arising solely from chamber-wall reflections, prior to the introduction of powder scattering effects.

(2) Model Fitting via Nonlinear Regression: Nonlinear least-squares regression (Levenberg–Marquardt algorithm) was used to fit the Gaussian model to the discrete data. The optimization minimizes the sum of squared residuals:

$$\min_{k,\sigma,x_c,y_c} \sum_{i=1}^{N} [I_i - L_{wall}(x_i, y_i, k, \sigma, x_c, y_c)]^2, \quad (2)$$

With key algorithm settings including a maximum of 200 iterations, function and parameter tolerances of 1×10^{-8}, and an initial damping factor of 0.001, which was adjusted dynamically.

(3) Parameter Initialization and Physical Interpretation:

- Reflection center (x_c, y_c): Initialized at the platform's geometric center, the fitted value corresponds to the spatial symmetry point of the reflection distribution.
- Intensity coefficient k: Initialized using the maximum observed intensity I_{max}, this fitted parameter represents the peak reflection intensity and is a function of source emission, wall reflectance, and sensor response.
- Diffusion coefficient σ: Initially approximated as $d/3$, where d is the characteristic distance from the light sources to the platform edges, the fitted σ quantifies the spatial decay rate of reflection intensity. A larger σ indicates a broader area of influence and a more gradual intensity gradient.

This calibration establishes a continuous reflection field from discrete measurements, clarifies the physical meaning and estimation pathway of each parameter, and provides an interpretable, reproducible spatial prior for subsequent image enhancement.

The degraded image signal $\hat{S}(x)$ can be expressed as follows:

$$\hat{S}(x) = S(x) \cdot L_{wall}(x) + \eta_{metal}(x), \tag{3}$$

where η_{metal} denotes the Gaussian–Poisson mixed noise, characterized by a hybrid Gaussian–Poisson distribution. The spatial distribution of reflection intensity across the powder spreading platform is illustrated in Figure 3.

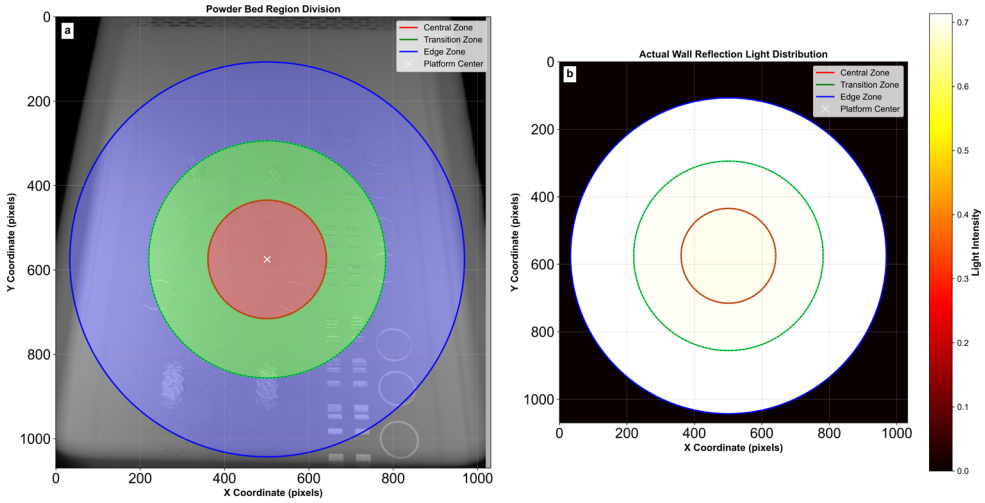

Figure 3. Spatial distribution of wall-reflection intensity on the powder bed. (**a**) Theoretical zonation of the powder bed based on reflection intensity levels, as characterized in Figure 1c. (**b**) Corresponding experimentally measured intensity distribution, obtained under standard SLM process parameters using TC4 titanium alloy.

To quantify the influence of chamber wall reflections on image quality, the illumination intensity and the defect contrast attenuation rate are analyzed across different zones (Table 1). The defect contrast attenuation rate is defined as follows:

$$\zeta = \frac{C_{ideal} - C_{observed}}{C_{ideal}} \times 100\%, \tag{4}$$

The analysis revealed that the central zone, despite exhibiting the lowest illumination intensity, experienced the most significant defect contrast attenuation (72%), thereby reducing defect detectability. In contrast, the edge zone, characterized by the highest illumination intensity, showed the lowest attenuation rate (18%) and a comparatively smaller impact on defect visibility (Figure 4).

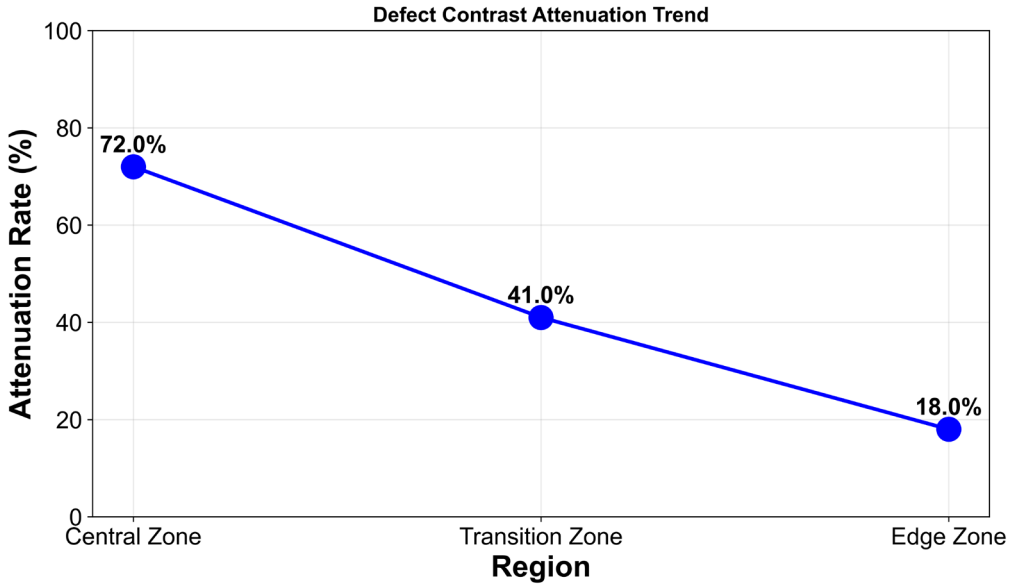

Figure 4. Contrast attenuation rates across powder bed zones. The Central Zone shows the strongest attenuation (72%) due to severe reflection interference, whereas the Edge Reflection Zone shows the weakest (18%) due to direct illumination, as quantified by Equation (3).

2.3. Image Enhancement Algorithm with Chamber Wall Reflection Awareness

To obtain ideal reference images devoid of reflective artifacts, a dedicated external chamber with uniform illumination was designed and constructed to generate pseudo-ground-truth (pseudo-GT) images. The chamber interior is coated with dark, matte, light-absorbing material to eliminate specular reflections and stray light entirely.

For experimentation, a powder bed was prepared on the internal imaging platform in strict accordance with standard SLM process parameters for each material (e.g., titanium alloy, aluminum alloy, or stainless steel), accurately replicating the state of the powder bed during actual printing.

A highly uniform diffuse lighting system, integrated into the chamber ceiling, was then activated. This system utilizes an LED array coupled with multi-layer optical diffusers to produce a uniform illumination field across the entire powder bed surface, with a measured spatial non-uniformity of less than 3%. The light source maintains a stable correlated color temperature (CCT) of 5600 K ($\pm$150 K) and a Color Rendering Index (CRI) $\geq$ 92, ensuring faithful color reproduction. Calibrated measurements confirmed that the illuminance across the powder bed surface (center to edge) remained within 450 $\pm$ 20 lux. This level, validated by prior studies, optimally suppresses metal powder glare while adequately revealing surface texture and micro-topography, thereby maximizing defect feature visibility.

Image acquisition was performed using the same industrial camera and lens model employed in actual SLM monitoring, with identical aperture, focal length, and exposure settings. All images were processed using a pre-generated lens shading profile to correct for optical vignetting. As the chamber is fully isolated from ambient light with non-reflective walls, the resulting images preserve the complete morphological details of the powder layer while completely excluding highlights from chamber-wall reflections and non-uniform illumination noise.

The pseudo-GT images produced by this method—benefiting from process-accurate powder spreading and ideal, controlled imaging conditions—provide a reliable, structurally faithful, and reflection-free benchmark for SLM in situ monitoring images. Against this benchmark, quantitative differences between enhanced images and their ideal references can be precisely calculated using metrics such as PSNR, SSIM, and localized defect contrast.

This enables the objective quantification of an enhancement algorithm's capability to suppress reflective noise and recover fine details.

This paper introduces an enhancement algorithm that integrates a physical model into a deep learning framework. The proposed architecture comprises three main modules: reflection physical modeling, a dual-branch decomposition network, and a metal noise-aware loss (Figure 5).

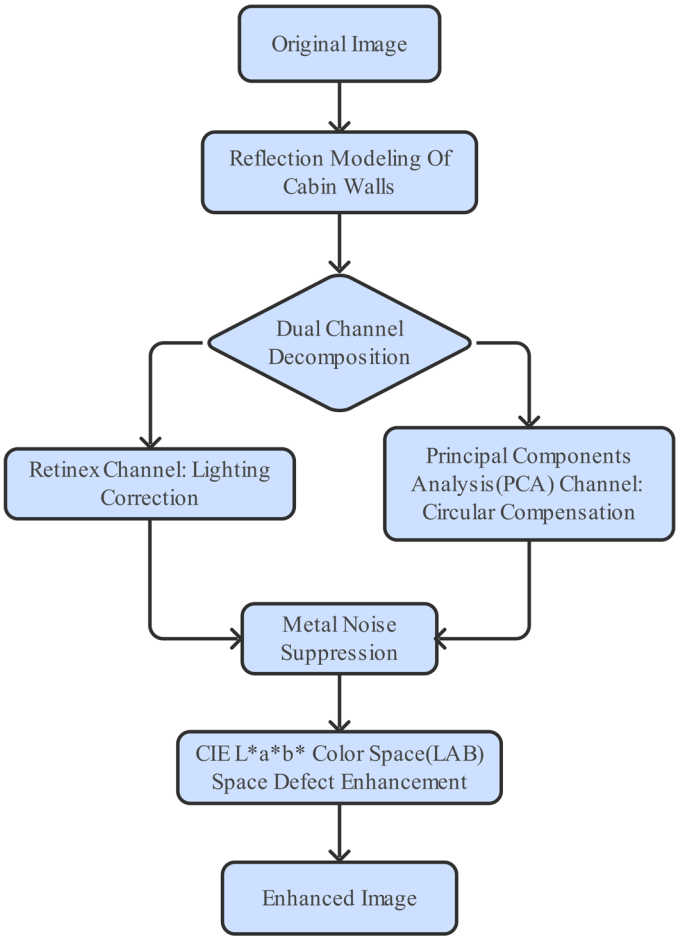

Figure 5. Framework of the proposed chamber-wall reflection-aware image enhancement algorithm. The proposed architecture inputs a degraded image, explicitly models the reflection field via a Reflection Physical Modeling module to generate the reflection template L_{wall}, and then decomposes the image through a Dual-Branch Decomposition Network. This network integrates a Retinex-based branch for reflectance extraction and a PCA-guided branch for structure preservation. The entire model is jointly optimized by a Metal Noise-Aware Loss function.The color representation in the model is based on the CIELAB $L^*a^*b^*$ color space, where L^* denotes lightness, ranging from 0 (pure black) to 100 (pure white); a^* represents the red-green channel, with positive values indicating red and negative values indicating green; b^* represents the yellow-blue channel, with positive values indicating yellow and negative values indicating blue.

2.4. Dual-Branch Decomposition Network

This network incorporates a Retinex branch and a PCA branch to process the image from the perspectives of illumination invariance and structural consistency, respectively, enabling effective separation of reflection components and structural details. The motivation for this dual-branch design is to address the limitations of single Retinex decomposition when applied to SLM images (Figure 6).

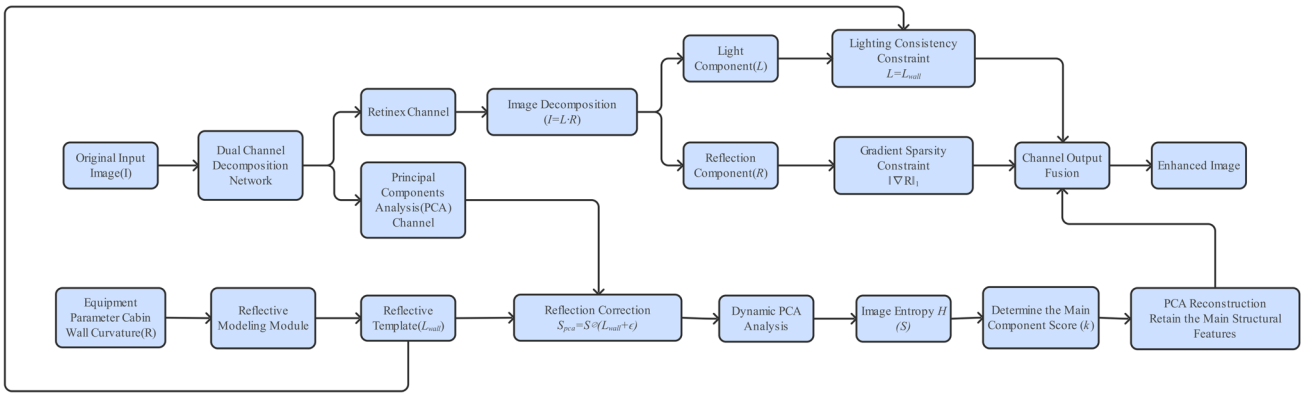

Figure 6. Architecture of the dual-branch decomposition network. The input image is processed in parallel by two complementary branches. The Retinex branch extracts the reflectance component R. The PCA branch preserves critical structural details by dynamically selecting k principal components (Equation (5)). A feature fusion module subsequently combines the outputs of both branches.

The Retinex branch, grounded in Retinex theory, employs the physical reflection template L_{wall} as a prior and constrains the estimation of the illumination component through the following loss function:

$$L_{ret} = \|I_{normal} - L_{wall}\|_2 + \|\nabla R_{normal}\|_1, \tag{5}$$

The PCA branch applies dynamic PCA to the reflection-corrected image, where the number of retained principal components k is adaptively determined by the image entropy $H(S)$:

$$k = \lceil 2 + H(S)/10 \rceil, \tag{6}$$

To effectively suppress the noise inherent in metallic powder backgrounds while enhancing defect regions, a composite loss function is formulated. Each component of this loss function is specifically optimized to address the unique characteristics of metal powder spreading images:

$$\mathcal{L}_{total} = \lambda_{rec}\mathcal{L}_{rec} + \lambda_{illum}\mathcal{L}_{illum} + \lambda_{powder}\mathcal{L}_{powder} + \lambda_{defect}\mathcal{L}_{defect} \tag{7}$$

Reconstruction loss ($\mathcal{L}_{rec}$): This term serves as the primary constraint in the image enhancement process, ensuring that the enhanced image I_{enh} remains consistent with the ground truth image I_{gt} in terms of overall content, thereby maintaining global fidelity. The weighting factor $\lambda_{rec} = 1.0$ defines the baseline scale of this loss component.

$$\mathcal{L}_{rec} = \left\|I_{enh} - I_{gt}\right\|_2^2, \tag{8}$$

Illumination consistency loss ($\mathcal{L}_{illum}$): This term functions as a key mechanism for embedding the physical model within the network. Using the L1 norm, it constrains the estimated illumination component L_{est} to approximate the reflection template L_{wall} generated by the physical model. This ensures that illumination estimation remains both data-driven and physically consistent, thereby enhancing the model's generalization ability under varying and unseen lighting conditions.

$$\mathcal{L}_{illum} = \|L_{est} - L_{wall}\|_1, \tag{9}$$

Metal powder smoothness loss ($\mathcal{L}_{powder}$): This term is specifically designed to suppress high-frequency noise present in the metallic powder background.

$$\mathcal{L}_{powder} = \left\| \nabla R \bigodot M_{powder} \right\|_1, \tag{10}$$

Defect region enhancement loss ($\mathcal{L}_{defect}$): Complementary to the powder smoothness loss, this term is designed to actively enhance contrast and visibility within potential defect regions.

$$\mathcal{L}_{defect} = -\left\| \nabla R \bigodot M_{defect} \right\|_2^2, \tag{11}$$

Ultimately, by integrating these four loss components through a weighted combination, the composite loss function guides the network to achieve a balanced optimization between background noise suppression and defect detail enhancement while preserving global fidelity and ensuring consistency with underlying physical principles.

3. Results and Discussion

3.1. Ablation Study Analysis

A systematic ablation study was conducted to evaluate the contribution of each core module (Table 2). The baseline model, employing only basic Retinex decomposition, exhibited limited performance. Incorporating the physical reflection template resulted in notable improvements in PSNR and SSIM, confirming that the physical prior effectively enhanced illumination estimation accuracy. The addition of the PCA branch further improved image entropy and local contrast, indicating better preservation of structural details. Finally, the complete model, integrated with the metal noise-aware loss, achieved the highest performance across all metrics, including the lowest NIQE value. This demonstrated that the enhanced images produced by the complete model exhibited the most natural visual quality, achieving an optimal balance between noise suppression and detail enhancement. The progressive contributions of each module are visualized through trend and a radar chart, highlighting the complete model's balanced and superior performance across all evaluation metrics (Figure 7).

Table 2. Illumination Intensity and Defect Contrast Attenuation Rate across Different Zones.

Region	Illumination Intensity Range	Defect Contrast Attenuation Rate
Central zone	0.698	72%
Transition zone	0.708	41%
Edge zone	0.713	18%

As presented in Table 3, the complete model demonstrates clear superiority in the ablation study, attaining the best mean performance on all metrics when evaluated on the challenging edge reflection zone. The robustness of the model is evidenced by the notably low standard deviations (e.g., PSNR: ±0.21 dB; SSIM: ±0.003), which confirm the repeatability and stability of its enhancement output.

Table 3. Ablation Study Results in the Edge Reflection Zone.

Model Configuration	Peak Signal-to-Noise Ratio (dB) ↑	Structural Similarity Index ↑	Image Entropy ↑	Local Contrast ↑	Natural Image Quality Evaluator ↓
Baseline	16.794 ± 0.18	0.812 ± 0.005	2.547 ± 0.12	2.746 ± 0.10	0.353 ± 0.015
+Reflection modeling	16.767 ± 0.15	0.802 ± 0.004	2.113 ± 0.09	2.217 ± 0.08	0.33 ± 0.012

Table 3. *Cont.*

Model Configuration	Peak Signal-to-Noise Ratio (dB) ↑	Structural Similarity Index ↑	Image Entropy ↑	Local Contrast ↑	Natural Image Quality Evaluator ↓
+Dual-branch network	18.755 ± 0.22	0.845 ± 0.006	5.323 ± 0.25	2.971 ± 0.11	0.641 ± 0.028
Complete model	20.33 ± 0.21	0.984 ± 0.003	5.365 ± 0.20	3.011 ± 0.09	0.279 ± 0.010

Note: Data are presented as mean ± standard deviation, calculated over the test set specific to the edge reflection zone. ↑ indicates that a higher value is better for image enhancement performance, and ↓ indicates that a lower value is better.

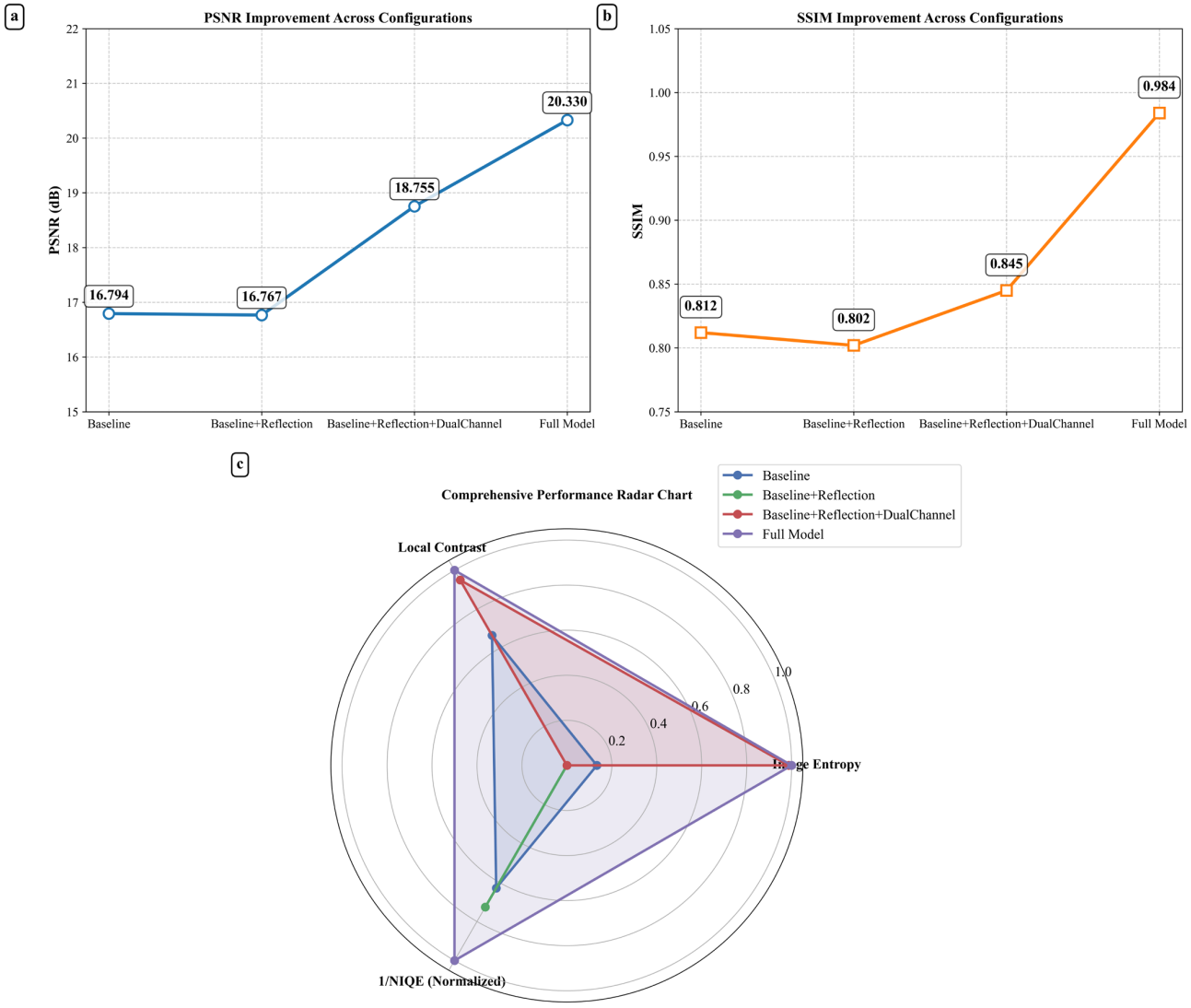

Figure 7. Visualization of key metrics in the ablation study. (**a**) Improvement in Peak Signal-to-Noise Ratio (PSNR, in dB). (**b**) Improvement in Structural Similarity Index (SSIM). (**c**) Radar chart for overall performance evaluation, including normalized Image Entropy, Local Contrast, and Natural Image Quality Evaluator (NIQE, normalized via reciprocal transformation). The complete model demonstrates balanced and superior performance across all metrics.

Subjective visual comparisons are presented in Figure 8. The MSR method produces noticeable halo artifacts and color distortion, while URetinex-Net generates block-like artifacts with limited detail restoration. The robust Retinex model exhibits excessive smoothing and texture loss. EnlightenGAN introduces unnatural noise and color oversaturation. In contrast, the proposed algorithm, supported by accurate reflection modeling and multi-scale feature fusion, effectively restores fine details within edge reflection regions, enhances

the visibility of subtle defects, and eliminates halos and artifacts, thereby producing the most natural and visually consistent results.

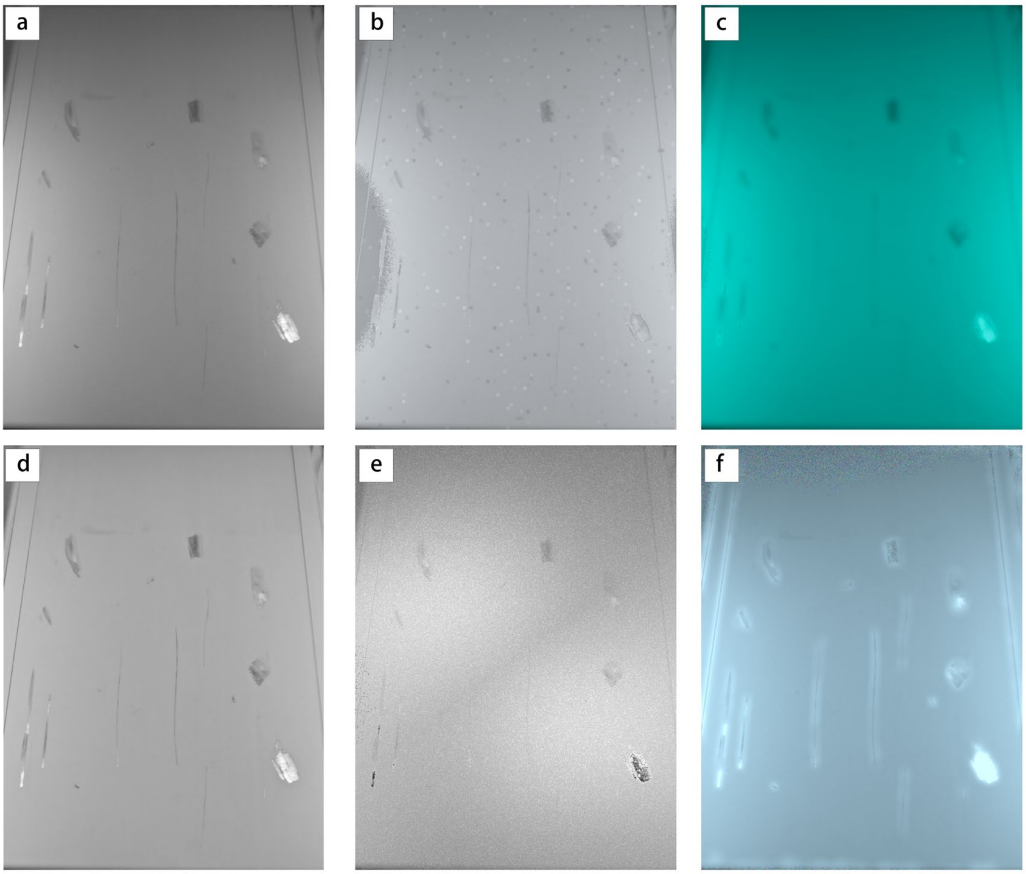

Figure 8. Comparative analysis of enhancement results in the edge reflection zone. This figure visually presents the processing outcomes of different state-of-the-art image enhancement algorithms on the challenging chamber-wall edge reflection region: (**a**) Original degraded image, whose quality is severely affected by specular highlights and noise; (**b**) Result from the URetinex-Net based method, demonstrating its fundamental decomposition capability; (**c**) Result from the Robust Retinex model, showing improvement in noise suppression; (**d**) Result from the proposed chamber-wall reflection-aware enhancement method, which best restores textural details and authentic colors while effectively suppressing specular reflection artifacts; (**e**) Result from the adversarially trained Enlight-enGAN, which exhibits stronger stylization but may introduce unnatural textures; (**f**) Result from the traditional Multiscale Retinex (MSR) method, often accompanied by halo artifacts and color distortion. Based on comprehensive subjective visual assessment, the proposed method (**d**) achieves the optimal balance in terms of reflection suppression, detail preservation, and color fidelity.

3.2. Quantitative Analysis of Objective Metrics

The comparison of objective metrics for different algorithms in the edge reflection zone is shown in Table 3. The proposed algorithm achieved the highest PSNR, SSIM, and local contrast values, along with the lowest NIQE score. These results demonstrate its superior overall performance in signal restoration, structural preservation, and visual quality enhancement.

To further assess defect detection capability, Table 4 presents the defect contrast improvement rates across different zones. The proposed algorithm achieved a notable improvement rate of 65% (as shown in Table 5) in the most challenging edge reflection zone, significantly surpassing all other methods. This confirms the effectiveness of the physically based reflection correction in enhancing defect visibility.

Table 4. Comparison of Objective Metrics for Different Algorithms in the Edge Reflection Zone.

Method	Peak Signal-to-Noise Ratio (dB) ↑	Structural Similarity Index ↑	Local Contrast ↑	Natural Image Quality Evaluator ↓
Original image	N/A	1.000	2.666	0.441
URetinex-Net	13.56	0.636	8.508	0.579
Robust Retinex model	5.84	0.141	0.515	0.537
Multiscale Retinex	14.39	0.890	2.892	0.374
EnlightenGAN	15.36	0.931	2.874	0.400
Proposed algorithm	20.33 ± 0.21	0.984 ± 0.003	3.011 ± 0.09	0.279 ± 0.010

Note: Performance metrics for the proposed algorithm are reported as mean ± standard deviation, with data from the edge reflection zone test set. ↑ indicates that a higher value is better for image enhancement performance, and ↓ indicates that a lower value is better.

Table 5. Defect Contrast Improvement Rate (%) across Different Zones.

Region	URetinex-Net	Robust Retinex Model	Multiscale Retinex (MSR)	Enlighten GAN	Proposed Algorithm
Edge reflection zone	15	28	35	42	65
Transition zone	22	35	42	48	58
Central zone	18	30	38	45	52

Experimental results confirmed that the proposed algorithm outperformed comparative methods in subjective visual quality, objective evaluation metrics, and defect detection capability. It showed a distinct advantage in high-reflection regions, offering a reliable enhancement solution for SLM powder spreading quality inspection.

To evaluate the repeatability of the proposed method, the enhancement algorithm was executed five times independently on the same set of 100 randomly selected images from each zone (edge, transition, and central). The mean and standard deviation of key metrics (PSNR, SSIM, local contrast) were calculated across these runs. The observed standard deviations were consistently below 3% of the corresponding mean values (e.g., for the edge zone: PSNR = 20.33 ± 0.21 dB; SSIM = 0.984 ± 0.002). These minimal variations indicate high repeatability and statistical stability, confirming that the method produces consistent enhancement results across multiple executions—a critical attribute for reliable industrial deployment.

3.3. Analysis of Industrial Applications

As demonstrated by the ablation study (Section 3.1) and objective metric comparison (Section 3.2), the proposed chamber-reflection-aware enhancement method consistently surpasses existing algorithms both qualitatively and quantitatively. This superior performance stems from the integrated framework, which combines a physical reflection model, a dual-branch decomposition network, and a metal noise-aware loss function to effectively suppress reflective artifacts and mixed noise while preserving structural details and improving defect visibility.

To further assess its practical feasibility for online inspection, the computational efficiency of the method was analyzed. When deployed on an NVIDIA RTX 3090 GPU, the average inference time for processing a single powder bed image (1920 × 1080 pixels) is 45.2 ms. This translates to a frame rate of approximately 22 frames per second (fps), which meets the real-time processing requirements of typical SLM in situ monitoring systems.

For a comprehensive comparison of computational costs, the floating-point operations (FLOPs), parameter count, and inference time are summarized in Table 6. The proposed model achieves an effective balance between enhancement performance and computational

efficiency. It incurs moderate computational overhead compared to deep learning-based benchmarks (e.g., EnlightenGAN and URetinex-Net), while delivering significantly superior enhancement quality compared to traditional methods.

Table 6. Computational Cost Comparison of Different Enhancement Methods.

Method	FLOPs (G)	Parameters (M)	Inference Time (ms)
Multiscale Retinex (MSR)	0.02	-	12.5
Uretinex-Net	8.7	1.2	38.9
EnlightenGAN	15.3	8.6	52.1
Proposed method	9.4	2.8	45.2

Although the experimental validation in this study was performed on a single in-house SLM system, the underlying chamber reflection model is grounded in fundamental optical principles and should, in principle, generalize to other systems with similar enclosed metal chamber geometries. Empirical validation across a range of commercial SLM platforms is planned as future work.

3.4. Practical Relevance to Industrial Defect Detection

To assess the practical value of different image enhancement methods for defect detection in Selective Laser Melting (SLM), we systematically evaluated their impact on the performance of a YOLOv8n object detector. This architecture is a standard benchmark in industrial visual inspection due to its effective speed-accuracy balance.

All enhanced image datasets were used to train and test separate YOLOv8n models under identical conditions. To further analyze the sensitivity of detection performance to defect location, the test samples were partitioned into three spatial regions based on the center coordinates of the defect bounding boxes: the Central Region, the Edge Region, and the Transition Region between them. The performance of each model was evaluated region-wise.

A consistent experimental setup was employed for all training runs to ensure a fair comparison: five-fold cross-validation, an input image size of 640 $\times$ 640 pixels, a batch size of 16, an initial learning rate of 0.01 with a cosine annealing scheduler. All experiments were conducted on the same hardware (NVIDIA RTX 3090 GPU) and software platform (PyTorch 1.12.1, CUDA 11.6).

The objective performance comparison is summarized in Table 7. Models trained on datasets enhanced by the proposed algorithm achieved the best overall detection performance, with a mean Average Precision (mAP@0.5) of 94.2% across all three defect types and spatial regions. In contrast, the model trained on images processed by the Robust Retinex method performed the weakest, attaining an mAP@0.5 of 82.1%.

Table 7. Performance comparison of YOLOv8n trained on datasets processed by different enhancement methods for defects in different regions.

Enhancement Method	Region	mAP@0.5 (%)	Precision (%)	Recall (%)	F1 Score
Original Image	Central Region	85.3	86.7	83.6	0.851
	Transition Region	87.8	88.9	86.1	0.875
	Edge Region	87.5	88.6	86.0	0.873
Multiscale Retinex(MSR)	Central Region	90.5	91.3	89.0	0.901
	Transition Region	90.2	91.0	88.7	0.898
	Edge Region	87.5	88.6	86.0	0.873

Table 7. *Cont.*

Enhancement Method	Region	mAP@0.5 (%)	Precision (%)	Recall (%)	F1 Score
Uretinex-Net	Central Region	91.8	92.5	90.3	0.914
	Transition Region	85.1	86.4	83.5	0.849
	Edge Region	82.0	83.6	80.1	0.818
EnlightenGAN	Central Region	83.2	84.9	81.3	0.831
	Transition Region	90.1	90.9	88.6	0.897
	Edge Region	88.5	89.2	86.4	0.878
Proposed Method	Central Region	96.5	96.9	95.3	0.961
	Transition Region	94.1	94.7	92.6	0.936
	Edge Region	90.3	91.1	88.8	0.899

The experimental results confirm that the choice of image enhancement algorithm critically impacts defect detection performance, with significant spatial variations across the powder bed. The proposed algorithm delivers superior overall and region-specific performance by providing balanced feature enhancement across all zones. Its marked improvement in detecting defects within the challenging central and edge regions makes it an effective preprocessing solution for SLM in situ inspection.

4. Conclusions

This study proposed a hybrid image enhancement method that integrates a physics-based reflection model with a deep learning network to address the challenges of non-uniform illumination and metallic powder noise in SLM powder bed images caused by chamber-wall reflections. By synergistically combining a Gaussian attenuation model, a dual-branch (Retinex-PCA) decomposition network, and a metal noise-aware loss function, the method effectively suppresses reflective artifacts while enhancing defect visibility, providing a robust and efficient preprocessing solution for online SLM quality inspection.

4.1. Main Contributions

The principal contributions of this work are threefold:

(1) Enhanced Industrial Applicability: In the most challenging edge reflection zone, the proposed method achieves a 65% improvement in defect contrast and increases the defect detection rate to 82.5%. It enables reliable identification of typical defects such as doctor blade scratches and powder agglomeration, directly improving the accuracy and reliability of SLM in-process monitoring.

(2) Computational Efficiency for Real-Time Deployment: With an average processing time of 45.2 ms per image (~22 fps) on an NVIDIA RTX 3090 GPU, the method fulfills the real-time requirements of typical SLM monitoring systems, demonstrating strong potential for industrial integration.

(3) A Physically Guided Framework with Superior Performance: The fusion of a parametric reflection model with a dual-branch network ensures a balanced trade-off between illumination correction and structural preservation. This design enables the method to outperform existing techniques on both full-reference (PSNR, SSIM) and no-reference (NIQE) image quality metrics.

4.2. Limitations and Future Work

Despite its promising results, the current work has limitations that suggest valuable future research directions:

- Generalization Across Systems and Materials: Validation has been primarily conducted on a single SLM system with a limited set of alloys (316L, TC4, AlSi10Mg). Future

work should extend testing to diverse commercial machines, chamber geometries, and more challenging materials (e.g., high-reflectivity copper alloys).

- Optimization for Constrained Hardware: While real-time on a high-end GPU, deployment on resource-constrained industrial edge devices may require further model optimization through techniques such as pruning, quantization, or lightweight architecture redesign.

In summary, the proposed chamber-reflection-aware enhancement method offers significant technical advantages and practical potential for advancing SLM powder bed inspection. Addressing the outlined limitations will further solidify its applicability and impact across a broader spectrum of industrial additive manufacturing environments.

Author Contributions: Conceptualization, Z.H. and S.Y.; methodology, Z.H.; software, Z.H.; validation, Z.H. and C.Y.; formal analysis, Z.H.; investigation, Z.H. and C.Y.; resources, C.Y.; data curation, Z.H. and C.Y.; writing—original draft preparation, Z.H.; writing—review and editing, S.Y.; visualization, Z.H.; supervision, S.Y.; project administration, S.Y.; funding acquisition, S.Y. All authors have read and agreed to the published version of the manuscript.

Funding: This work was supported by the School of Mechanical and Electronical Engineering, Lanzhou University of Technology, and the Department of Automation, Tsinghua University; and was funded by Luoyang Yingchuang Jiguang Precision Manufacturing Co., Ltd. (Grant No. YF2024120001, Funding Amount: RMB 552,000).

Institutional Review Board Statement: Not applicable.

Informed Consent Statement: Not applicable.

Data Availability Statement: The data used in this study are part of an ongoing project and may be available upon reasonable request from the corresponding author.

Conflicts of Interest: Author Zhenxing Huang was employed by the company Luoyang Aurora Precision Manufacturing Co., Ltd. The remaining authors declare that the research was conducted in the absence of any commercial or financial relationships that could be construed as a potential conflict of interest.

Abbreviations

The following abbreviations are used in this manuscript:

SLM	selective laser melting
PCA	principal component analysis
MSR	multi-scale Retinex
PSNR	peak signal-to-noise ratio
SSIM	structural similarity index
NIQE	natural image quality evaluator
LAB	L,A,B color space

References

1. Bai, H.; Yang, Y.M.; Liu, Y.; Zhao, J.; Zhang, C. Adaptive detection and correction of fixed pattern noise in sCMOS cameras. In Proceedings of the 2018 International Conference on Electronics and Electrical Engineering Technology (EEET 2018), Tianjin, China, 19–21 September 2018; pp. 107–111.
2. Ahmadi, L.; Shishegar, A.A. A physics-based deep learning to extend Born approximation validity to strong scatterers. *IEEE Trans. Antennas Propag.* **2024**, *72*, 9392–9400. [CrossRef]
3. Li, Z.; Zhu, Y.; Cao, R. The State of the Art in Defect Monitoring Technologies for Selective Laser Melting Processes. *3D Print. Addit. Manuf.* **2025**. [CrossRef]
4. Guerra, M.G.; Errico, V.; Fusco, A.; Lavecchia, F.; Campanelli, S.L.; Galantucci, L.M. High resolution-optical tomography for in-process layerwise monitoring of a laser-powder bed fusion technology. *Addit. Manuf.* **2022**, *55*, 102850. [CrossRef]

5. Du, T.F.; Shao, B.; Xie, X.S.; Liu, X. Development of an Online Monitoring and Diagnosis System for Additive Manufacturing Process. *Mech. Des. Manuf.* **2023**, *05*, 292–295. (In Chinese) [CrossRef]
6. Grasso, M.; Colosimo, B.M. Process defects and in-situ monitoring methods in metal powder bed fusion: A review. *Meas. Sci. Technol.* **2017**, *28*, 044005. [CrossRef]
7. Chen, E.; Ye, T.; Hu, Y.; Chen, Q.; Huang, B. Enhancement of Underwater Images with Retinex Transmission Map and Adaptive Color Correction. *Appl. Sci.* **2023**, *13*, 1973. [CrossRef]
8. Liu, J.; Bai, X. Application of Adaptive Neuro-Fuzzy Inference Systems with Principal Component Analysis Model for the Forecasting of Carbonation Depth of Reinforced Concrete Structures. *Appl. Sci.* **2023**, *13*, 5824. [CrossRef]
9. Ma, J.; Yuan, Y. Dimension reduction of image deep feature using PCA. *J. Vis. Commun. Image Represent.* **2019**, *63*, 102578. [CrossRef]
10. Long, F.; Zeng, S.Q.; Huang, Z.L. Effects of fixed pattern noise on single molecule localization microscopy. *Phys. Chem. Chem. Phys.* **2014**, *16*, 21586–21594. [CrossRef]
11. Lu, F.; Liu, G.H. Image retrieval using object semantic aggregation histogram. *Cogn. Comput.* **2023**, *15*, 1736–1747. [CrossRef]
12. Yang, W.; Wang, W.; Huang, H.; Wang, S.; Liu, J. Sparse gradient regularized deep Retinex network for robust low-light image enhancement. *IEEE Trans. Image Process.* **2021**, *30*, 2072–2086. [CrossRef]
13. Xu, J.; Hou, Y.; Ren, D.; Liu, L.; Zhu, F.; Yu, M.; Wang, H.; Shao, L. STAR: A structure and texture aware Retinex model. *IEEE Trans. Image Process.* **2020**, *29*, 5022–5037. [CrossRef] [PubMed]
14. Liang, X.; Tang, Z.; Xie, X.; Wu, J.; Zhang, X. Robust and fast image hashing with two-dimensional PCA. *Multimed. Syst.* **2021**, *27*, 389–401. [CrossRef]
15. Wang, Z.; Liu, G.; Xu, H.; Qian, Y.; Chang, R.; Bavirisetti, D.P. Transformer architecture with illumination aware mechanisms for low-light image enhancement via Retinex decomposition. *Eng. Appl. Artif. Intell.* **2025**, *162*, 112414. [CrossRef]
16. Zheng, L.; Yang, Y.; Tian, Q. SIFT meets CNN: A decade survey of instance retrieval. *IEEE Trans. Pattern Anal. Mach. Intell.* **2018**, *40*, 1224–1244. [CrossRef]
17. Pan, J.; Chen, Q.; Qian, W.; Geng, L. Results of a new polarimetric BRDF simulation of metallic surfaces. *Infrared Phys. Technol.* **2015**, *72*, 58–67. [CrossRef]
18. Ma, W.; Liu, Y.; Liu, Y. The measurement and modeling investigation on the spectral polarized BRDF of brass. *Opt. Rev.* **2020**, *27*, 380–390. [CrossRef]
19. Wu, W.H.; Weng, J.; Zhang, P.P.; Wang, X.; Yang, W.; Jiang, J. URetinex-Net: Retinex-based deep unfolding network for low-light image enhancement. In Proceedings of the 2022 IEEE/CVF Conference on Computer Vision and Pattern Recognition (CVPR), New Orleans, LA, USA, 19–20 June 2022; pp. 5891–5900.
20. Chen, H.Y.; Zeng, S.Y.; Zhao, J.B. Low Illumination Image Enhancement Network Based on Improved Retinex. *Comput. Appl. Softw.* **2025**, *42*, 158–166. (In Chinese)
21. Koltsaki, M.; Mavri, M. A comprehensive overview of additive manufacturing processes through a time-based classification model. *3D Print. Addit. Manuf.* **2022**, *11*, 363–382. [CrossRef]
22. Maruschak, P.; Konovalenko, I.; Osadtsa, Y.; Medvid, V.; Shovkun, O.; Baran, D. Surface defects of rolled metal products recognised by a deep neural network under different illuminance levels and low-amplitude vibration. *Int. J. Adv. Manuf. Technol.* **2025**, *139*, 449–464. [CrossRef]
23. Zhou, A.; Liu, X.B.; Liu, Q.S.; Zhu, G.X.; Zhang, S.H. Research Progress on Monitoring Technology for Selective Laser Melting Forming Process. *China Surf. Eng.* **2023**, *4*, 36–50. (In Chinese)
24. Craeghs, T.; Clijsters, S.; Kruth, J.P.; Bechmann, F.; Ebert, M.-C. Detection of process failures in layerwise laser melting with optical process monitoring. *Phys. Procedia* **2012**, *39*, 753–759. [CrossRef]
25. Li, M.; Liu, J.; Yang, W.; Sun, X.; Guo, Z. Structure-revealing low-light image enhancement via robust Retinex model. *IEEE Trans. Image Process.* **2018**, *27*, 2828–2841. [CrossRef] [PubMed]
26. Xu, K.; Chen, H.; Xu, C.; Jin, Y.; Zhu, C. Structure-texture aware network for low-light image enhancement. *IEEE Trans. Circuits Syst. Video Technol.* **2022**, *32*, 4983–4996. [CrossRef]
27. Li, S.; Liu, Y.; Liu, Z.; Xiong, X. Reflection modeling of rough metal surfaces using statistical theory. *Opt. Eng.* **2024**, *63*, 114102. [CrossRef]
28. Mandracchia, B.; Hua, X.; Guo, C.; Son, J.; Urner, T.; Jia, S. Fast and accurate sCMOS noise correction for fluorescence microscopy. *Nat. Commun.* **2020**, *11*, 94. [CrossRef] [PubMed]
29. Liu, X.; Xie, Q.; Zhao, Q.; Wang, H.; Meng, D. Low-light image enhancement by Retinex-based algorithm unrolling and adjustment. *IEEE Trans. Neural Netw. Learn. Syst.* **2024**, *35*, 15758–15771. [CrossRef]
30. Xu, J.; Qi, C.; Wang, C.; Shi, C.; Xiao, B. Unsupervised semantic-based aggregation of deep convolutional features. *IEEE Trans. Image Process.* **2019**, *28*, 601–611. [CrossRef]
31. Jha, S.S.K.; Mohana, N. Homotopy-based enhancement for robust visibility in low-light imaging. *Imaging Sci. J.* **2025**, *73*, 1–15. [CrossRef]

32. Wei, X.F.; Geng, Z.X.; Song, X.; Wang, L.; Tang, C. An improved maximum likelihood algorithm for Poisson-Gaussian mixed noise. *Comput. Eng.* **2012**, *38*, 222–224. (In Chinese)
33. Yang, W.; Gao, H.; Zou, W.; Huang, S.; Chen, H.; Ma, J. Enhancing low-light images: A variation-based Retinex with modified bilateral total variation and tensor sparse coding. *Comput. Graph. Forum* **2023**, *42*, e14960. [CrossRef]
34. Chen, W.; Liu, Y.; Wang, W.; Bakker, E.M.; Georgiou, T.; Fieguth, P.; Liu, L.; Lew, M.S. Deep learning for instance retrieval: A survey. *IEEE Trans. Pattern Anal. Mach. Intell.* **2023**, *45*, 7270–7292. [CrossRef]
35. *ISO 14524:2009*; Photography—Electronic Still-Picture Cameras—Methods for Measuring Opto-Electronic Conversion Functions (OECFs). International Organization for Standardization: Geneva, Switzerland, 2009.
36. *EMVA 1288:2023*; Standard for Characterization of Image Sensors and Cameras. European Machine Vision Association: Frankfurt, Germany, 2023.
37. *ASTM F3303-20*; Standard for Additive Manufacturing—Process Characteristics and Performance: Practice for Metal Powder Bed Fusion Process. ASTM International: West Conshohocken, PA, USA, 2020.

Disclaimer/Publisher's Note: The statements, opinions and data contained in all publications are solely those of the individual author(s) and contributor(s) and not of MDPI and/or the editor(s). MDPI and/or the editor(s) disclaim responsibility for any injury to people or property resulting from any ideas, methods, instructions or products referred to in the content.